

Nanoenabled Direct Contact Interfacing of Syringe-Injectable Mesh Electronics

Jung Min Lee,^{†,‡,§,#} Guosong Hong,^{†,§,#} Dingchang Lin,^{†,§,#} Thomas G. Schuhmann, Jr.,[‡] Andrew T. Sullivan,[‡] Robert D. Viveros,[‡] Hong-Gyu Park,^{*,‡,§,ID} and Charles M. Lieber^{*,†,‡,§,ID}

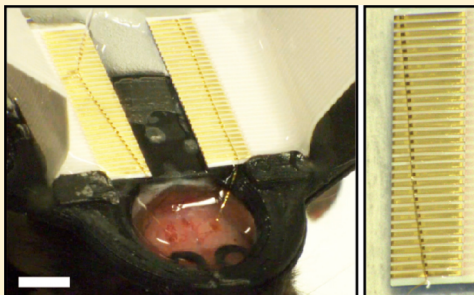
[†]Department of Chemistry and Chemical Biology, [‡]John A. Paulson School of Engineering and Applied Sciences, and [§]Center for Brain Science, Harvard University, Cambridge, Massachusetts 02138, United States

[#]Department of Physics, Korea University, Seoul 136701, Republic of Korea

^{*}Department of Materials Science and Engineering, Stanford University, Stanford, California 94305, United States

S Supporting Information

ABSTRACT: Polymer-based electronics with low bending stiffnesses and high flexibility, including recently reported macroporous syringe-injectable mesh electronics, have shown substantial promise for chronic studies of neural circuitry in the brains of live animals. A central challenge for exploiting these highly flexible materials for *in vivo* studies has centered on the development of efficient input/output (I/O) connections to an external interface with high yield, low bonding resistance, and long-term stability. Here we report a new paradigm applied to the challenging case of injectable mesh electronics that exploits the high flexibility of nanoscale thickness two-sided metal I/O pads that can deform and contact standard interface cables in high yield with long-term electrical stability. First, we describe the design and facile fabrication of two-sided metal I/O pads that allow for contact without regard to probe orientation. Second, systematic studies of the contact resistance as a function of I/O pad design and mechanical properties demonstrate the key role of the I/O pad bending stiffness in achieving low-resistance stable contacts. Additionally, computational studies provide design rules for achieving high-yield multiplexed contact interfacing in the case of angular misalignment such that adjacent channels are not shorted. Third, the *in vitro* measurement of 32-channel mesh electronics probes bonded to interface cables using the direct contact method shows a reproducibly high yield of electrical connectivity. Finally, *in vivo* experiments with 32-channel mesh electronics probes implanted in live mice demonstrate the chronic stability of the direct contact interface, enabling consistent tracking of single-unit neural activity over at least 2 months without a loss of channel recording. The direct contact interfacing methodology paves the way for scalable long-term connections of multiplexed mesh electronics neural probes for neural recording and modulation and moreover could be used to facilitate a scalable interconnection of other flexible electronics in biological studies and therapeutic applications.



KEYWORDS: Double-sided metal input/output, flexible input/output, multiplexed electrophysiology, biocompatible neural probes, chronic neural interface, flexible electronics

Unraveling the complexity of the brain requires the development of tools capable of bridging a wide range of spatial and temporal scales, from tens of nanometers of individual synapses to centimeters of interconnected regions of the brain and from the millisecond duration of single action potentials to long-term changes associated with development, learning, memory, and disease over months to years,^{1–3} respectively. Implantable electrophysiology probes have been widely explored in this context,^{4–6} with current silicon-based electronics^{4,7–12} and metallic microwire electrodes^{13–16} demonstrating single-neuron spatial and temporal resolutions with recent high-electrode-density Si probes^{7–9} further showing these capabilities in recording from hundreds to thousands of neurons simultaneously. Nevertheless, these rigid neural recording technologies have exhibited limited chronic stability due to the chronic immune response and relative shear

motion at the probe–tissue interface resulting from a mechanical mismatch with soft neural tissue.^{17–19} Thus, tracking the evolution of circuitry relevant to understanding many critical neural functions requires new implantable probe technologies with substantial improvements in the duration of stable neural recording.⁴

Recently, we introduced a new paradigm for implantable neural probes termed mesh electronics that are designed to look and feel like the neural tissue they are designed to probe.^{20–27} Mesh electronics probe design features include three-dimensional (3D) open macroporous structure, low bending stiffness comparable to that of neural tissue, and

Received: July 23, 2019

Revised: July 30, 2019

Published: July 30, 2019

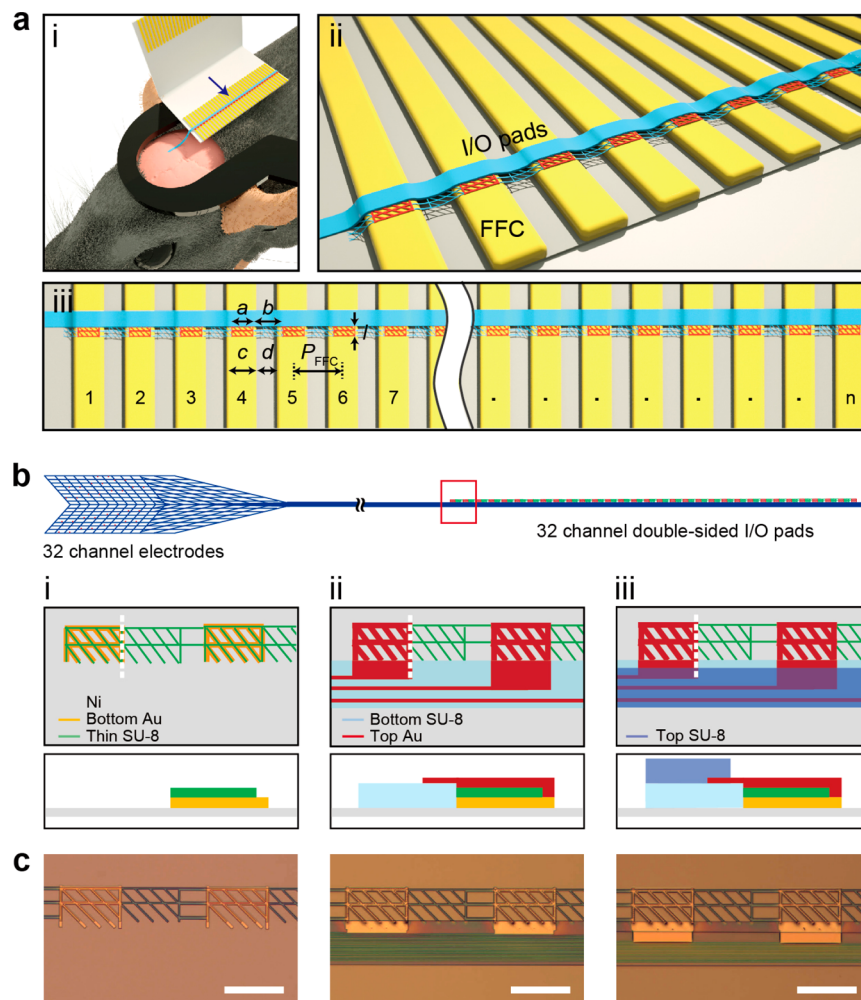


Figure 1. Overview of the direct contact input/output (I/O) interface for syringe-injectable mesh electronics. (a) Schematics illustrating the concept of the direct contact I/O interface. (i) Mesh electronics (blue) implanted into the mouse brain (pink), with the I/O portion of the mesh ejected over and electrically connected to the metal leads (gold) of an FFC, where the FFC is bonded to a head stage (black) glued to the mouse skull. (ii) Close-up view of the I/O interface indicated by the blue arrow in (i), where double-sided metal I/O pads (red) directly contact the FFC metal leads (gold) and are encapsulated by an insulating polymer polymer. (iii) Scalability of the direct contact interface, where n indicates the number of I/O pads on the mesh probe in simultaneous contact with n metal leads on the FFC or other instrument interface. Here we focus on $n = 32$. Design parameters a , b , c , d , l , and P_{FFC} correspond to the width of the I/O pad, the gap between neighboring I/O pads, the width of metal FFC leads, the gap between neighboring metal FFC leads, the length of the I/O pad, and the pitch of the FFC defined as $P_{\text{FFC}} = c + d = a + b$, respectively. (b) Schematic of the 32-channel mesh electronics neural probe, highlighting (left) the mesh structure with neural recording electrodes, (middle) parallel interconnects, and (right) corresponding double-sided I/O pads. Key fabrication steps of I/O pads are shown in close-up views in the red box: (i) Bottom Au pads (orange) are fabricated on the Ni sacrificial layer (gray), with the thin SU-8 layer (green) patterned on top of and connecting the bottom Au pads. (ii) The bottom passivation layer of SU-8 (light blue) is patterned. Parallel metal interconnects are fabricated on this layer and connect to the top Au pads (red), which are fabricated on top of the bottom Au/thin SU-8. (iii) The top passivation layer of SU-8 (darker blue) is fabricated to encapsulate the metal interconnects but leave the bottom/top (double-sided) I/O pads exposed. The bottom row of diagrams shows corresponding side-view structures along the white vertical dashed lines in the top row. (c) Bright-field microscopy images of the fabrication steps corresponding to the schematics in (b) for design III discussed in the text and Figure 2. Scale bars are 200 μm .

feature sizes similar to those of neuron somata and axons.^{4,20,21,23,26} These design features have been shown to yield unique biocompatibility^{5,18,28,29} as characterized by a minimal long-term chronic immune response and seamless integration between the electronic and neural networks, thereby enabling stable long-term recording and tracking of the same single neurons on at least a yearly time scale. In addition, there has been considerable effort by other research groups developing flexible electronics for recording from neural and other tissues.^{4,5,18,30–42}

In the case of the implanted mesh electronics probes, it has been especially challenging to obtain multiplexed recording

given the challenges in interfacing the mesh electronics probe input/output (I/O) connections with the recording and stimulation instrumentation because these I/O connections are made after the injection process used to implant electronics.^{19,43,44} Specifically, studies to date^{20–22,25,26} have injected ultraflexible mesh electronics probes through small capillary needles to targeted regions of the brain, leaving the top end of the I/O pads exposed for electrical connection to an external recording interface after the entire mesh is ejected from the needle. Conventional I/O bonding techniques such as soldering,⁴⁵ wire bonding,⁴⁶ and anisotropic conductive films⁴⁷ are, however, incompatible with intraoperative

connection because of the submillimeter-scale I/O pads and high temperature and pressure conditions necessary for these methods. Approaches used to overcome these obstacles for the facile implementation of mesh electronics probes have included computerized but serial conductive ink printing^{21,22,25,26} and a parallel plug-and-play I/O interface.⁴³ Despite the practical success of these approaches, limitations including (i) a long processing time depending on the number of connection channels, (ii) the risk of electrical shorts between neighboring contacts, (iii) structural constraints to achieving multiplexed connection without breaking the metal interconnects during clamping with the zero insertion force (ZIF) connectors, and (iv) the need for specific orientation of the I/O pads have created a barrier to the implementation of the attractive properties of mesh electronics by other laboratories.

To address these limitations, we asked whether it would be possible to design and implement a new facile approach for forming highly multiplexed and misalignment-tolerant electrical connections between the mesh electronics neural probe I/O and the external interface for large-scale and long-term brain mapping at the single-neuron level. Our overall concept addressing this question in Figure 1a schematically illustrates the connection of the I/O portion of the mesh electronics to a standard flat-flexible cable (FFC) instrument interface following syringe-based implantation in the brain and highlights several key design points. First, to facilitate the overall surgery the FFC or other interface is fixed to a head stage that is glued to the animal's skull prior to implantation (Figure 1a,i). When the I/O portion of the mesh probe is ejected over FFC metal contacts, we reasoned that a critical advance would be the integration of "two-sided" connection pads so that the orientation at which they exit the capillary needle does not affect making metal-to-metal contacts. Indeed, the necessity of orienting single-sided I/O pads in the plug-and-play methodology⁴³ represents one significant weakness of this previously reported connection scheme. Second, the bending stiffness or flexibility of the individual I/O pads should be critical to their deformation and formation of low resistance connections to FFC metal leads (Figure 1a,ii) without any additional heat or pressure. Third, the design of the size and pitch of the double-sided I/O pads with respect to the width and pitch of the corresponding metal leads on an FFC or related instrument interface (Figure 1a,iii) allows for high-yield scalable connections that are tolerant of misalignment. We set $a = P_{\text{FFC}} - c$, where a is the width of the I/O pads, P_{FFC} is the pitch of the metal leads of the FFC, and c is the width of the metal leads in the FFC, by specifically considering the ideal case where the array of mesh I/O pads is perfectly aligned with the FFC metal leads as shown in Figure 1a. This choice of parameters prevents electrical shorting for this ideal case without any rotational misalignment (Materials and Methods, Supporting Information). In addition, by controlling the length, l , of the I/O pad, it is also possible to design a tolerance for rotational misalignment (i.e., the stem with I/O pads is oriented at an angle with respect to the metal leads which differs from the ideal perpendicular configuration) without shorting the adjacent channels (Materials and Methods, Supporting Information).

To explore the critical design features described above, we have investigated a 32-channel mesh, where our previous studies have focused primarily on 16-channel designs given challenges in reliable I/O interfacing.^{21,25,26} The overall mesh

electronics probes are designed with three distinct functional regions (Figure 1b, Figure S1a, and Figure S2, top): the mesh device region that comprises exposed Pt recording electrodes (Figure 1b, left; Figure S1b; and Figure S2,i); a stem region which contains parallel metal interconnects between the electrodes and the I/O pads (Figure 1b, middle; Figure S1c; Figure S2,ii); and the I/O region, which provides an electrical interface to the external recording instrument (Figure 1b, right; Figure S1d; Figure S2,iii). The latter region represents the focus and unique enabling advance in the present work.

The design constraints for the I/O pads discussed above were explored in studies of direct contact interfacing to a standard FFC (Figure 1a), where the FFC leads have a width, c , and pitch, P_{FFC} , of 300 and 500 μm, respectively, with the gap between adjacent metal leads, d , being 200 μm. For these interface parameters, the width and gap of the mesh I/O pads (a and b , Figure 1a,iii) were designed to match those of the FFC leads with the following relationships: $a = d = 200 \mu\text{m}$ and $b = c = 300 \mu\text{m}$ (Figure 1a,iii). For an I/O pad length (l) that is one-half the gap between FFC leads, 100 μm, we carried out analyses to determine the maximum angular displacement of the mesh stem relative to the ideal perpendicular alignment with respect to the direction of the FFC interface leads before electrical shorts can occur between adjacent channels (Materials and Methods, Supporting Information; Figure S3). These results that are summarized in Figure S3 have several key points. First, by setting the width of I/O pads, a , equal to the gap of the FFC metal leads, d , with the same pitch, there are no electrical shorts at 0° rotational misalignment regardless of where along the horizontal axis the I/O pads are centered. Second, decreasing l from c to $d/2$ reduces the propensity for shorting between adjacent leads. For rotational misalignments of as large as 15°, no more than two I/O pads cause shorting for any angle, while for the longer I/O pads, where $l = c$, as many as five consecutive I/O pads can be shorted at once. Third, by positioning the first I/O pad at the center of the first FFC lead in both dimensions, there is no shorting for any angular misalignment value for which all of the pads are on the FFC (i.e., for all angles of between ±7°). Therefore, by choosing the I/O pad design parameters as described above, our method is capable of forming a reliable electrical interface with FFC leads that is tolerant of misalignment over a relatively wide range of angles without producing shorting between adjacent channels.

Critical to facile connection in these studies is the implementation of flexible I/O pads consisting of a mesh structure for flexibility with exposed gold contact surfaces on both sides, termed "double-sided" I/O pads, such that contacts to the instrument interface (FFC leads in our studies) can be made with either orientation of the I/O pad side (i.e., top or bottom) facing the interface following ejection from the capillary needle (Figure S4). The key steps involved in the fabrication of flexible double-sided Au mesh I/O pads are as follows (Figure 1b,i–iii; Materials and Methods, Supporting Information). First, 100-nm-thick Au mesh pads with 10-μm-wide elements were patterned on a Ni sacrificial layer as the bottom I/O electrical contacts. Second, a 200-nm-thick SU-8 layer was patterned with a mesh structure consisting of 6-μm-wide elements that overlap with but are smaller than the bottom Au mesh pads and provide structural elements between these pads (Figure 1b,i). This thin SU-8 layer is also important in matching the heights of the I/O pad and the bottom SU-8 layer of the stem region, which is patterned in a subsequent

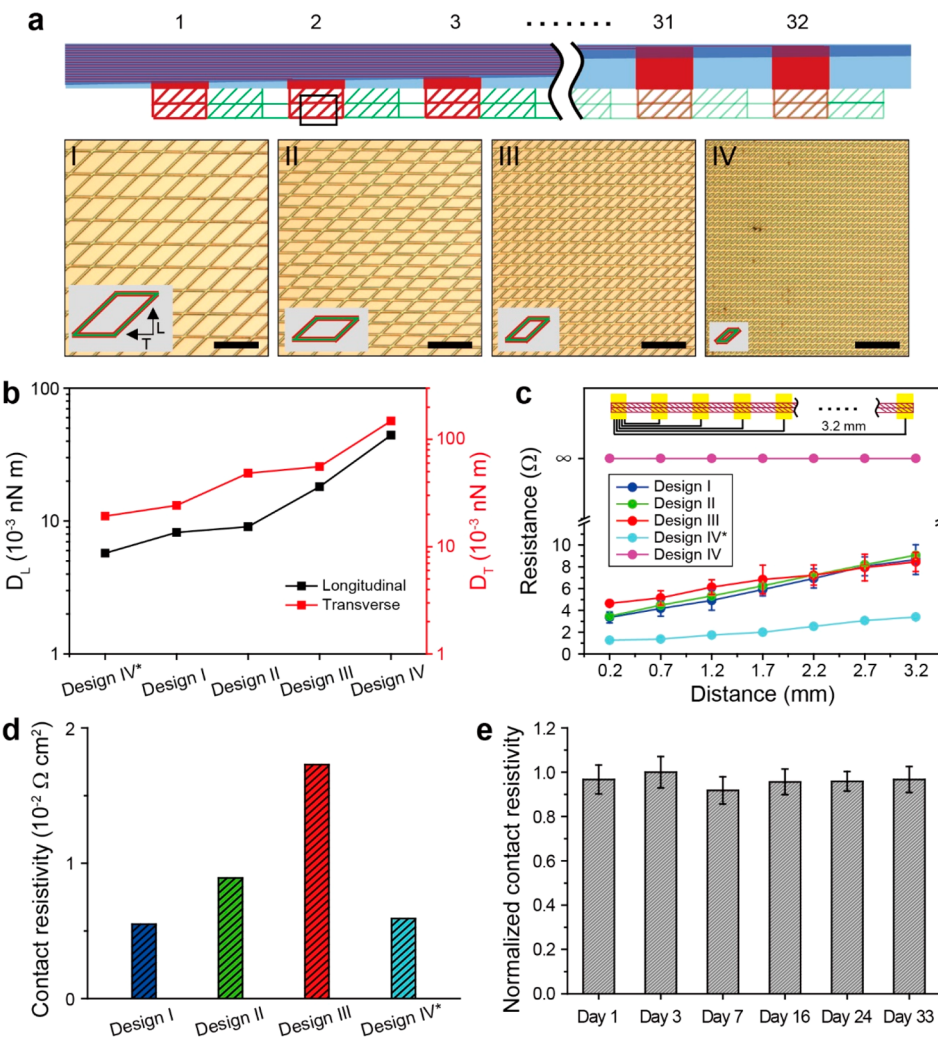


Figure 2. Designs and properties of direct contact I/O pads. (a) (Top) Schematic of 32-channel direct contact I/O pads. (Bottom) Optical microscopy images of four I/O pad designs (designs I–IV) with different unit-cell sizes. Two different I/O pads are made for IV, where design IV* has the same in-plane geometry as design IV but the total thickness is halved (ca. 150 nm for design IV* vs 300 nm for design IV). Scale bars are 200 μm . The insets show the schematics of the corresponding unit cells. (b) Simulated bending stiffness for the longitudinal (D_L , left y axis) and transverse directions (D_T , right y axis) for the five I/O pad designs: I, II, III, IV, and IV*. (c) Measured pairwise resistance values for the five I/O pad designs as a function of the distance between two FFC leads, on which a continuous mesh I/O pad is mounted (top schematic). Error bars denote ± 1 standard deviation (SD). (d) Contact resistivities are defined as the contact resistance, R_c (1.16, 1.27, 2.02, and 0.34 Ω), derived from the extrapolated y intercepts in (c), multiplied by ideal contact areas, A_c (0.004, 0.006, 0.008, and 0.012 cm^2), based on the unit cells of designs I, II, III, and IV*. (e) Measured contact resistivity of design III over 1 month, normalized against the maximum value from the chronic measurements. A single-factor ANOVA test was used to determine if there was a significant change in the mean contact resistivity over time, which yields a p value of 0.9142, suggesting that there is no statistically significant change in contact resistivity over at least 1 month. Error bars denote ± 1 SD.

step defining the bottom layer of the overall mesh probe. Third, the Au interconnects and top I/O pads are patterned such that the top and bottom I/O pads are electrically connected to each other and to their corresponding interconnects and electrode channels of the mesh probe (Figure 1b,ii). Finally, a top SU-8 passivation layer is fabricated to insulate the Au interconnects, leaving the recording electrodes and both sides of the I/O pads exposed, thereby enabling the formation of electrical contacts on both sides of the I/O pads (Figure 1b,iii). Optical microscopy images (Figure 1c) show these three key steps of fabrication corresponding to the schematics in Figure 1b. We note that the flexible double-sided Au I/O pads for the direct contact interface can be easily fabricated in this manner by conventional 2D photolithography, thus enabling the rapid testing of key parameters relevant to robust interface connections and

allowing for straightforward scaling of the number and density of I/O pads to match the instrumentation interface leads.

To determine optimal structural parameters for I/O pads (Figure 2a, top schematic), we first investigated the correlation between the bending stiffness and contact resistivity for two-sided mesh I/O pads following direct connection to interface metal leads. The contact resistivity was measured after ejecting a continuous mesh I/O pad onto the leads of a 32-channel FFC interface, allowing the aqueous solution to evaporate, and then measuring the resistance between pairs of FFC leads separated by distances ranging from 0.2 to 3.2 mm. Four distinct unit-cell sizes were examined (Figure 2a,I–IV; Figure S5a), where the mesh structures in these designs have Au/SU-8/Au layers with thicknesses of 100/100/100 nm, respectively. In addition, a fifth design, IV*, was considered with the same

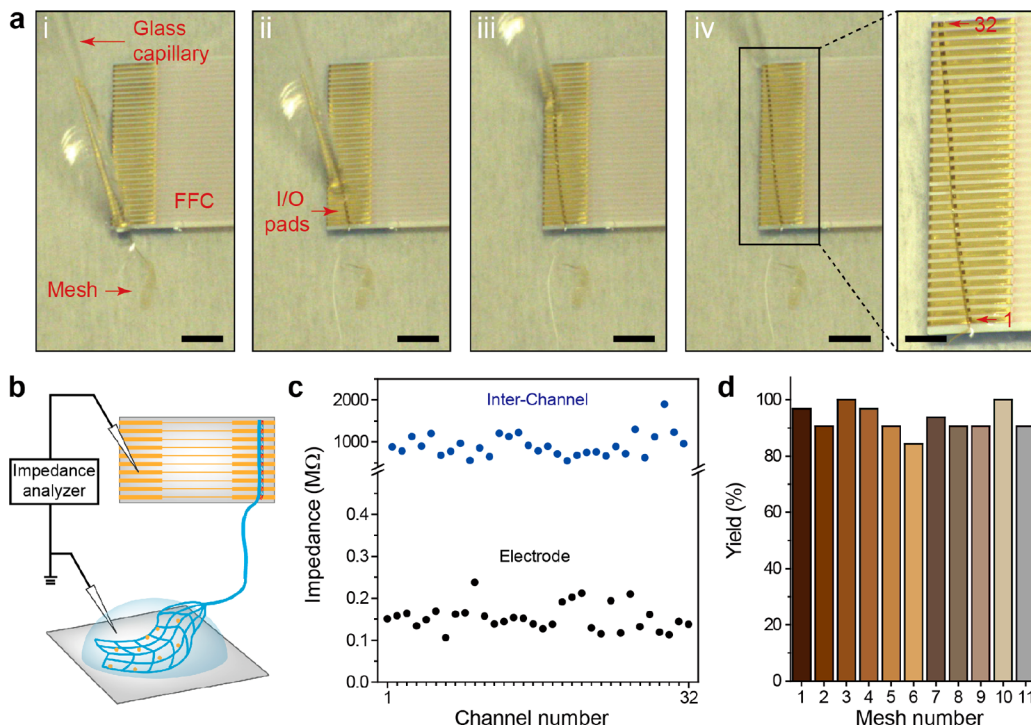


Figure 3. In vitro demonstration and characterization of the direct contact I/O interface. (a) A series of optical microscopy images (i to iv) showing the electrical connection of mesh I/O pads to the FFC via the direct contact I/O interface. Scale bars are 4 mm. (Right) Close-up image of the black box in (iv), which shows 100% alignment of the I/O pads with FFC metal leads (32 out of 32 channels). The scale bar is 2 mm. (b) Schematic of impedance measurement, where 1× phosphate-buffered saline (PBS) solution covers the recording electrode region of the mesh electronics to complete the circuit for the impedance measurement. (c) Measured in vitro electrode (black dots) and interchannel (blue dots) impedance values at 1 kHz for a 32-channel mesh. The electrode and interchannel impedance values were measured as described in the Materials and Methods, Supporting Information. (d) Yields of electrical connection of eleven 32-channel meshes with the direct contact I/O interfaces.

unit cell as for IV but reduced Au/SU-8/Au layer thicknesses of 50/50/50 nm, respectively (Figure S5b).

First, we asked how the bending stiffness of the I/O pads would be expected to vary for these different designs. To answer this question, we carried out finite element analyses to calculate the longitudinal (D_L) and transverse (D_T) bending stiffness values for the five mesh designs with the different in-plane geometries, designs I to IV, and thicknesses, design IV* (Materials and Methods, Supporting Information). Notably, the simulation results (Figure 2b) show systematic increases in the longitudinal and transverse bending stiffness values for $(0.57\text{--}4.4) \times 10^{-2}$ and $(1.9\text{--}15) \times 10^{-2}$ nN·m, respectively. With respect to our five distinct structural designs, the smallest D_L and D_T values correspond to design IV* due to the reduced layer thicknesses, while designs I to IV show progressive increases in these values due to their decreasing unit-cell sizes.

Second, we asked how these systematic changes in mechanical stiffness affect the quality of the electrical interface between I/O pads and the FFC leads. We measured the resistance as a function of distance between pairs of FFC leads for the different pad designs to obtain the contact resistance (R_c), where only the intrinsic capillary force, which arises during solution evaporation, is used to form the electrical contacts in all cases. Significantly, these data (Figure 2c) show small resistances of $<10\ \Omega$ for designs I, II, III, and IV*, with a ca. linear increase in the measured resistance with contact separation (from 0.2 to 3.2 mm). In contrast, no electrical connection was observed for the stiffest I/O pad, design IV, showing that flexibility plays a critical role in forming low-resistance contacts during aqueous solution evaporation.

To better define the electrical characteristics of the successful contacts, we calculated the contact resistivity, which is defined as the contact resistance normalized by the conductor area because the contact area varies for the different unit-cell sizes of the designs. A summary of these results (Figure 2c,d) demonstrates that there is a direct relationship between the I/O pad bending stiffness and the contact resistance with values of 0.34, 1.2, 1.3, and $2.0\ \Omega$ for designs IV*, I, II, and III, respectively, and corresponding contact resistivities of 0.59×10^{-2} , 0.55×10^{-2} , 0.89×10^{-2} , and $1.73 \times 10^{-2}\ \Omega\cdot\text{cm}^2$, respectively, where the smallest bending stiffness designs, I and IV*, yield the smallest contact resistivities. All four of these designs have reasonably low resistivity values of $<2 \times 10^{-2}\ \Omega\cdot\text{cm}^2$, although we selected design III as the mesh I/O pad for subsequent experiments because it is somewhat more robust mechanically. Comparing these results to previous mesh electronics interfacing studies^{20,43,44} shows that the highest baseline contact resistance of the four designs, $2.0\ \Omega$, is still comparable to the recent plug-and-play contact resistance, ca. $3\ \Omega$,⁴³ and is 10–1000 times smaller than values reported for the anisotropic conductive film²⁰ and conductive ink,⁴⁴ 34 and $4200\ \Omega$, respectively.

Third, to make an initial assessment of the potential of the direct contact I/O interface for long-term multiplexed brain mapping in live animals, we evaluated the stability of the mesh I/O interface of design III with the mesh and FFC mounted on the head stage of a live mouse but without brain implantation. The mesh I/O pads were connected to the FFC leads and passivated with epoxy, and the contact resistivity was evaluated

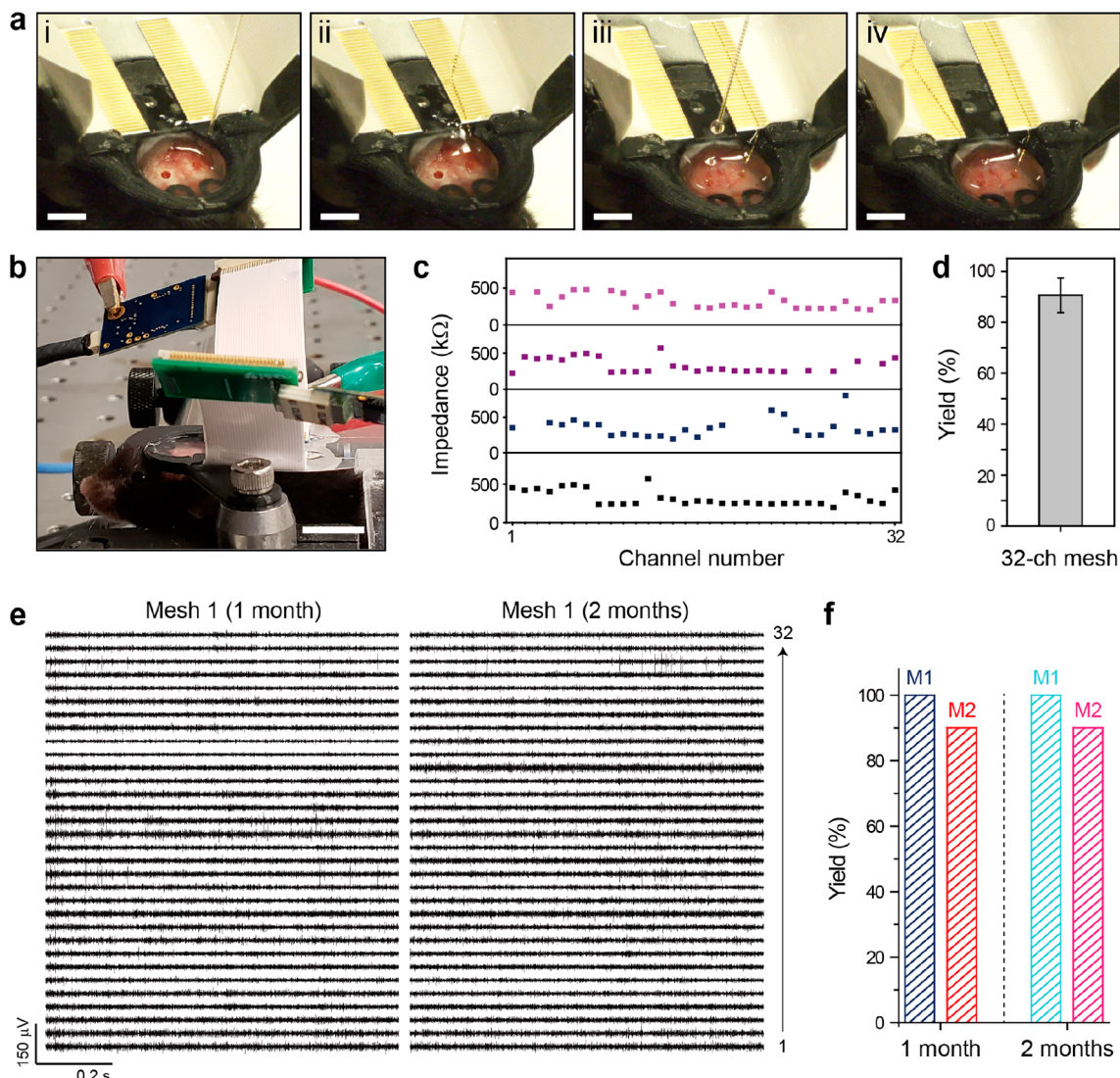


Figure 4. In vivo demonstration of the direct contact I/O interface. (a) Images showing the alignment and direct contact connection of I/O pads to the two FFCs fixed on the mouse head stage. The mesh electronics probes were injected into the hippocampus of both cerebral hemispheres. (b) Image of a head-fixed mouse while recording from both implanted mesh probes, which were connected to the FFCs by the direct contact method. Instrument amplifiers are attached to each of the FFC interfaces for the recording session and are visible in the upper portion of the image. The scale bar is 4 mm. (c) Measured in vivo impedance values at 1 kHz for four 32-channel implanted mesh probes. Channels for which no impedance value is shown were disconnected, with impedance values $>2\text{ M}\Omega$. (d) Yield of the electrical connection of the 32-channel meshes ($N = 4$). The error bar denotes $\pm 1\text{ SD}$ (e) 32-channel neural recordings from Mesh 1 at 1 month (left) and 2 months (right) postinjection. (f) Yields for electrical connection of the two 32-channel mesh probes (Mesh 1 in Figure 4e and Mesh 2 in Figure S6) at 1 month and 2 months postinjection.

over the course of 1 month (Materials and Methods, Supporting Information). A comparison of the normalized contact resistivity over 33 days (Figure 2e) demonstrates that the I/O pad-to-FFC lead interface is stable without any statistically significant changes over this 1-month period. We address below the chronic stability of mesh electronics probes with direct contact I/O interfaces that are implanted in the brains of mice.

To quantify the functional connection yield of multichannel direct contact I/O interfaces, we performed an in vitro impedance measurement with 32-channel mesh electronics probes, where the I/O pads of the probes are connected to FFC interface leads and the mesh electrodes are immersed in phosphate-buffered saline (PBS; Materials and Methods, Supporting Information). The impedance of the Pt-recording electrodes, which, on the basis of previous studies, should have

values in the range of 200–600 kΩ,^{21,26} can serve as a good measure of I/O contacts because a high-resistance contact or shorted contacts would lead to anomalously large or small impedance values, respectively. Sequential images (Figure 3a) and Supporting Information Video 1 highlight the process of ejecting the mesh electronics I/O pads onto the leads of the FFC and the formation of the direct contact interface with key steps as follows. First, the FFC was fixed on a glass slide with dental cement, and oxygen plasma treatment was carried out to render the FFC surface hydrophilic (Figure 3a,i). After loading the entire mesh probe into a 1.1-mm-inner-diameter (i.d.) glass pipet from deionized (DI) water (Materials and Methods, Supporting Information), the device region with recording electrodes was first ejected onto the glass slide, followed by the I/O pad region, which was carefully positioned on the FFC leads (Figure 3a,ii and iii). If the I/O pads were misaligned

with respect to FFC leads (i.e., alignment angle $>10^\circ$; [Figure S3](#)), then the I/O pads were pulled back into the capillary by applying negative pressure and were ejected onto the FFC metal leads until an alignment angle of $<10^\circ$ was achieved. Finally, the remaining DI water was removed with spear sponges and the bonded I/O interface was left to dry naturally for 5–10 min ([Materials and Methods, Supporting Information](#)). A representative example showing good alignment with a 100% connection yield of 32-channel I/O pads to the underlying 32 FFC leads, despite the presence of small angular misalignment between the rows of I/O pads and FFC leads, is shown in [Figure 3a,iv](#).

The reproducibility of the direct contact interface for functional measurements was tested by characterizing the impedance of the mesh probe recording electrodes in 1× PBS as shown in [Figure 3b](#), where each of the 32 recording electrodes was tested independently through the FFC output connections ([Materials and Methods, Supporting Information](#)). A representative interfacial impedance measurement at 1 kHz for a 32-channel mesh probe ([Figure 3c](#), lower black points) shows a 100% yield of electrical connection with the impedance values of all channels of less than ca. 200 kΩ. We have also addressed the functional reproducibility of the direct contact interface by carrying out measurements on 10 additional 32-channel meshes (11 in total). These data, which are summarized in [Figure 3d](#), show that 328 out of 352 channels (ca. 93%) have successful electrical connection to the FFC in the in vitro impedance measurement. Additionally, to investigate potential electrical cross-talk of the direct contact interface, interchannel impedances between adjacent Au interconnects were characterized ([Figure 3c](#), upper blue points), with values of ca. 1 GΩ consistent with an absence of shorting or partial shorting of the direct contact I/O connections. Finally, interchannel impedance measurements made in the same manner from 3 meshes with 96 channels in total yield an average impedance of ca. 1 GΩ \pm 0.4 GΩ (\pm 1 SD), thus confirming the absence of shorting or partial shorting and the overall reliability for the direct contact interface.

Next, we asked whether it would be possible to use the direct contact I/O interfacing paradigm for facile and robust chronic electrophysiological recording from the brains of live mice. To this end, we carried out chronic in vivo experiments testing the implantation and connection of two 32-channel mesh electronics probes in the left and right hippocampal regions of the same mouse brain ([Materials and Methods, Supporting Information](#)). The procedure for direct contact I/O interfacing in live animals is a straightforward adaptation of our in vitro methods described above and shown in [Figure 4a](#) ([Supporting Information Video 2 and Supporting Information](#)) with several key points. First, the head stage with 2 FFCs affixed, where the 32 exposed metal leads are oriented anterior–posterior (AP) on the 2 sides adjacent to the central opening of the stage, was fixed to the exposed skull with dental cement ([Figure 4a,i](#)). The FFC surface was wetted with sterile DI water to maintain its hydrophilicity. Second, a mesh electronics probe was injected into the hippocampus using the field of view (FoV) method, and the needle was withdrawn during the injection,⁴⁴ keeping the I/O pads inside the needle. Using the motorized stereotaxic frame to drive the needle, the two-sided I/O pads were roughly positioned over the FFC leads and ejected, and the I/O pads were then aligned with the row of FFC leads ([Figure 4a,ii](#)). The above steps were repeated

for the injection of the second mesh probe in the opposite hemisphere of the brain ([Figure 4a,iii,iv](#)). The entire process is also shown in [Supporting Information Video 2](#). The time required for I/O connection during surgery is only 5–10 min for each 32-channel interface connection, which represents a significant time savings compared to previous printing methods,^{21,22,26} and the I/O interface is very compact because of the elimination of connectors³⁰ that are otherwise needed for the instrument interface.

To assess the stability of the direct contact I/O interface, we carried out multiplexed electrophysiological recording in a head-fixed configuration over a two-month period. In brief, for each recording session the mouse was brought from the animal facility, the head-stage was screwed to a stage to fix the animal's head position and the free end of the FFC was connected to the amplifier/digitizer of the recording instrument through a standard PCB interface ([Figure 4b](#); [Materials and Methods, Supporting Information](#)). Initially, we characterized the yield of functional electrical connections postimplantation by measurement of the impedance of each of the recording electrodes at 1 kHz 2 h after implantation. The measured in vivo impedance values and yields of two 32-channel probes implanted in two mice ([Figure 4c,d](#)) show several important points. First, the direct contact interface can be applied to in vivo electrophysiological recording with facile interfacing. Second, the direct contact interface exhibits a mean in vivo impedance value of ca. 320 kΩ, which is the same order of magnitude as the in vitro impedance value of ca. 200 kΩ ([Materials and Methods, Supporting Information](#)). Finally, this method shows a connection yield of ca. 90% between the external interface and recording electrodes from four meshes implanted into the brain (116 out of 128 channels).

With this basic in vivo connection information in hand, we asked about the ability to record multiplexed single neuron activity over extended periods of time, where chronic single unit stability has been a unique advantage of mesh electronics demonstrated primarily for 16-channel probes previously.^{21,25,26} Representative 32-channel data from 2 probes implanted in the right/left hippocampal regions of a mouse at 1 and 2 months ([Figure 4e](#); [Figure S6a](#)) highlight several key points. First, multiplexed electrophysiology traces show the stable recording of characteristic extracellular action potentials from neurons over 2 months using the direct contact interface. Second, 32 and 8 representative channels with sorted spikes from meshes 1 and 2, respectively, show similar waveforms at 1 and 2 months postinjection, which confirms the chronic stability of not only the interface between the mesh probe and the brain tissue but also the direct contact interface between the mesh probe and external recording instrumentation ([Figure S6b](#); [Figure S7](#)). Third, the majority of channels recorded neural activity from two or three neurons on average, with the total number of 102 single units recorded 1 month postinjection and 107 single units recorded 2 months postinjection from the 40 representative channels in meshes 1 and 2. No channels exhibited a decrease in the number of recorded single units during this time period. Finally, no disconnection of channels from 1 month to 2 months postinjection in either mesh was observed, which confirms the chronic stability of the electrical interface between the I/O pads and FFC produced through the direct contact method ([Figure 4f](#)).

In conclusion, our results demonstrate the ability of double-sided I/O pads to form a chronically stable, high-yield

electrical interface between syringe-injectable mesh electronics and an external recording instrumentation interface in a facile and reproducible manner. In contrast to conventional I/O bonding techniques^{45,46} and previous I/O interfacing with mesh electronics,^{21,43} our direct contact method makes electrical connections to the external interface by the capillary-force-induced deformation of I/O pads without any additional pressure or heating. We have described the design and facile fabrication of two-sided metal I/O pads that allow for contact without regard to probe orientation, carried out systematic studies demonstrating that the contact resistance is determined directly by I/O pad design and mechanical properties, and provided design rules for achieving high-yield multiplexed contact interfacing in the case of angular misalignment without the shorting of adjacent channels. In particular, optimal design nanoscale-thickness double-sided metal I/O pads yielded $<2 \times 10^{-2} \Omega \cdot \text{cm}^2$ contact resistivity regardless of the side of the pad in contact with a standard FFC instrument interface and functional connection yields of at least 90% in *in vitro* and *in vivo* studies. In addition, multiplexed *in vivo* electrophysiological recording data show clear single-unit action potentials, which were confirmed by spike sorting of the data, and demonstrate chronic stability of the electrical interface between the I/O pads and FFC using the direct contact interface over a period of at least 2 months. These results thus suggest that leveraging the chronically stable facile direct contact I/O interface with the ability of mesh electronics to seamlessly integrate with surrounding neural tissue and track single-neuron activity up to at least a year^{21,25,26} could pave the way for reliable multiplexed recording that can uncover complex circuit evolution underlying processes such as learning, memory, and age-dependent neurodegeneration. Finally, the direct contact interface provides a pathway for significantly increasing the multiplexity of mesh electronics electrodes while maintaining a high electrical connection yield and ease of interface formation. This potential arises from the generality of our I/O pad design concept, which can be adapted to the needs of the target external interface using conventional 2D lithography processes. Furthermore, the direct contact I/O interface provides a new paradigm for electrical connection in other flexible electronics platforms^{30–42} and thus could impact areas beyond the specific application of stable single-neuron tracking in neuroscience.

■ ASSOCIATED CONTENT

§ Supporting Information

The Supporting Information is available free of charge on the ACS Publications website at DOI: [10.1021/acs.nanolett.9b03019](https://doi.org/10.1021/acs.nanolett.9b03019).

Materials and methods; overall design of mesh electronics neural probes; 32-channel mesh with double-sided I/O pads for direct contact; design of I/O pad geometry to prevent the shorting of adjacent channels; double-sided I/O pad geometry for facile alignment on FFC; I/O pad unit-cell designs for optimizing contact resistivity; chronically stable recordings of a second implanted mesh; spike sorting of recorded electrical traces to identify single units ([PDF](#))

In vitro I/O pad alignment on FFC ([MOV](#))

In vivo I/O pad alignment on FFC following mesh injection ([MOV](#))

■ AUTHOR INFORMATION

Corresponding Authors

*E-mail: hgpark@korea.ac.kr.
*E-mail: cml@cmliris.harvard.edu.

ORCID

Hong-Gyu Park: [0000-0002-6375-0314](https://orcid.org/0000-0002-6375-0314)

Charles M. Lieber: [0000-0002-6660-2456](https://orcid.org/0000-0002-6660-2456)

Author Contributions

#These authors contributed equally to this work.

Notes

The authors declare no competing financial interest.

■ ACKNOWLEDGMENTS

C.M.L. acknowledges the support of this work by the Air Force Office of Scientific Research (FA9550-18-1-0469) and an NIH Director's Pioneer Award (SDP1EB025835-02). This material is based upon work supported by the National Science Foundation Graduate Research Fellowship Program under grant nos. DGE1144152 and DGE1745303 (R.D.V.). H.-G.P. acknowledges the support of this work by a National Research Foundation of Korea (NRF) grant funded by the Korean government (MSIP) (no. 2018R1A3A3000666). G.H. acknowledges the support of this work by American Heart Association Postdoctoral Fellowship 16POST27250219 and a National Institutes of Health Pathway to Independence Award (NIA SR00AG056636-04). T.G.S.J. acknowledges support by the Department of Defense (DoD) through the National Defense Science & Engineering Graduate Fellowship (NDSEG) program. This work was performed in part at the Harvard University Center for Nanoscale Systems (CNS), a member of the National Nanotechnology Coordinated Infrastructure Network (NNCI), which is supported by the National Science Foundation.

■ REFERENCES

- (1) Herry, C.; Johansen, J. P. *Nat. Neurosci.* **2014**, *17*, 1644–1667.
- (2) Geva-Sagiv, M.; Las, L.; Yovel, Y.; Ulanovsky, N. *Nat. Rev. Neurosci.* **2015**, *16*, 94–108.
- (3) Moser, E. I.; Moser, M.-B.; McNaughton, B. L. *Nat. Neurosci.* **2017**, *20*, 1448–1464.
- (4) Hong, G.; Lieber, C. M. *Nat. Rev. Neurosci.* **2019**, *20*, 330–345.
- (5) Feiner, R.; Dvir, T. *Nat. Rev. Mater.* **2018**, *3*, 17076.
- (6) Lacour, S. P.; Courtine, G.; Guck, J. *Nat. Rev. Mater.* **2016**, *1*, 16063.
- (7) Jun, J. J.; Steinmetz, N. A.; Siegle, J. H.; Denman, D. J.; Bauza, M.; Barbarits, B.; Lee, A. K.; Anastassiou, C. A.; Andrei, A.; Aydin, Ç. *Nature* **2017**, *551*, 232–236.
- (8) Steinmetz, N. A.; Koch, C.; Harris, K. D.; Carandini, M. *Curr. Opin. Neurobiol.* **2018**, *50*, 92–100.
- (9) Raducanu, B. C.; Yazicioglu, R. F.; Lopez, C. M.; Ballini, M.; Putzeys, J.; Wang, S.; Andrei, A.; Rochus, V.; Welkenhuysen, M.; Helleputte, N. V.; Musa, V.; Puers, R.; Kloosterman, F.; Hoof, C. V.; Fiáth, R.; Ulbert, I.; Mitra, S. *Sensors* **2017**, *17*, 2388.
- (10) Rios, G.; Lubenov, E. V.; Chi, D.; Roukes, M. L.; Siapas, A. G. *Nano Lett.* **2016**, *16*, 6857–6862.
- (11) Fiáth, R.; Beregszászi, P.; Horváth, D.; Wittner, L.; Aarts, A. A.; Ruther, P.; Neves, H. P.; Bokor, H.; Acsády, L.; Ulbert, I. *J. Neurophysiol.* **2016**, *116*, 2312–2330.
- (12) Hochberg, L. R.; Serruya, M. D.; Friehs, G. M.; Mukand, J. A.; Saleh, M.; Caplan, A. H.; Branner, A.; Chen, D.; Penn, R. D.; Donoghue, J. P. *Nature* **2006**, *442*, 164–171.
- (13) Hafting, T.; Fyhn, M.; Molden, S.; Moser, M.-B.; Moser, E. I. *Nature* **2005**, *436*, 801–806.

- (14) Quiroga, R. Q.; Reddy, L.; Kreiman, G.; Koch, C.; Fried, I. *Nature* **2005**, *435*, 1102–1107.
- (15) Schwarz, D. A.; Lebedev, M. A.; Hanson, T. L.; Dimitrov, D. F.; Lehew, G.; Meloy, J.; Rajangam, S.; Subramanian, V.; Ifft, P. J.; Li, Z.; Ramakrishnan, A.; Tate, A.; Zhuang, K. Z.; Nicolelis, M. A. L. *Nat. Methods* **2014**, *11*, 670–676.
- (16) Okubo, T. S.; Mackevicius, E. L.; Payne, H. L.; Lynch, G. F.; Fee, M. S. *Nature* **2015**, *528*, 352–357.
- (17) Salatino, J. W.; Ludwig, K. A.; Kozai, T. D.; Purcell, E. K. *Nat. Biomed. Eng.* **2017**, *1*, 862–877.
- (18) Chen, R.; Canales, A.; Anikeeva, P. *Nat. Rev. Mater.* **2017**, *2*, 16093.
- (19) Rivnay, J.; Wang, H.; Fenno, L.; Deisseroth, K.; Malliaras, G. G. *Sci. Adv.* **2017**, *3*, No. e1601649.
- (20) Liu, J.; Fu, T.-M.; Cheng, Z.; Hong, G.; Zhou, T.; Jin, L.; Duvvuri, M.; Jiang, Z.; Kruskal, P.; Xie, C.; Suo, Z.; Fang, Y.; Lieber, C. M. *Nat. Nanotechnol.* **2015**, *10*, 629–636.
- (21) Fu, T.-M.; Hong, G.; Zhou, T.; Schuhmann, T. G.; Viveros, R. D.; Lieber, C. M. *Nat. Methods* **2016**, *13*, 875–882.
- (22) Fu, T.-M.; Hong, G.; Viveros, R. D.; Zhou, T.; Lieber, C. M. *Proc. Natl. Acad. Sci. U. S. A.* **2017**, *114*, E10046–E10055.
- (23) Hong, G.; Yang, X.; Zhou, T.; Lieber, C. M. *Curr. Opin. Neurobiol.* **2018**, *50*, 33–41.
- (24) Hong, G.; Viveros, R. D.; Zwang, T. J.; Yang, X.; Lieber, C. M. *Biochemistry* **2018**, *57*, 3995–4004.
- (25) Hong, G.; Fu, T.-M.; Qiao, M.; Viveros, R. D.; Yang, X.; Zhou, T.; Lee, J. M.; Park, H.-G.; Sanes, J. R.; Lieber, C. M. *Science* **2018**, *360*, 1447–1451.
- (26) Yang, X.; Zhou, T.; Zwang, T. J.; Hong, G.; Zhao, Y.; Viveros, R. D.; Fu, T.-M.; Gao, T.; Lieber, C. M. *Nat. Mater.* **2019**, *18*, 510–517.
- (27) Dai, X.; Hong, G.; Gao, T.; Lieber, C. M. *Acc. Chem. Res.* **2018**, *51*, 309–318.
- (28) Green, J. J.; Elisseeff, J. H. *Nature* **2016**, *540*, 386–394.
- (29) Sadtler, K.; Singh, A.; Wolf, M. T.; Wang, X.; Pardoll, D. M.; Elisseeff, J. H. *Nat. Rev. Mater.* **2016**, *1*, 16040.
- (30) Jiang, Y.; Li, X.; Liu, B.; Yi, J.; Fang, Y.; Shi, F.; Gao, X.; Sudzilovsky, E.; Parameswaran, R.; Koehler, K.; Nair, V.; Yue, J.; Guo, K. H.; Fang, Y.; Tsai, H.-M.; Freyermuth, G.; Wong, R. C. S.; Kao, C.-M.; Chen, C.-T.; Nicholls, A. W.; Wu, X. Y.; Shepherd, G. M. G.; Tian, B. *Nat. Biomed. Eng.* **2018**, *2*, 508–521.
- (31) Jiang, Y.; Tian, B. *Nat. Rev. Mater.* **2018**, *3*, 473–490.
- (32) Shi, E.; Li, H.; Yang, L.; Hou, J.; Li, Y.; Li, L.; Cao, A.; Fang, Y. *Adv. Mater.* **2015**, *27*, 682–688.
- (33) Guan, S.; Wang, J.; Gu, X.; Zhao, Y.; Hou, R.; Fan, H.; Zou, L.; Gao, L.; Du, M.; Li, C.; Fang, Y. *Sci. Adv.* **2019**, *5*, No. eaav2842.
- (34) Feiner, R.; Engel, L.; Fleischer, S.; Malki, M.; Gal, I.; Shapira, A.; Shacham-Diamand, Y.; Dvir, T. *Nat. Mater.* **2016**, *15*, 679–685.
- (35) Yin, R.; Xu, Z.; Mei, M.; Chen, Z.; Wang, K.; Liu, Y.; Tang, T.; Priydarshi, M. K.; Meng, X.; Zhao, S.; Deng, B.; Peng, H.; Liu, Z.; Duan, X. *Nat. Commun.* **2018**, *9*, 2334.
- (36) Zhang, J.; Liu, X.; Xu, W.; Luo, W.; Li, M.; Chu, F.; Xu, L.; Cao, A.; Guan, J.; Tang, S.; Duan, X. *Nano Lett.* **2018**, *18*, 2903–2911.
- (37) Kim, D.-H.; Viventi, J.; Amsden, J. J.; Xiao, J.; Vigeland, L.; Kim, Y.-S.; Blanco, J. A.; Panilaitis, B.; Frechette, E. S.; Contreras, D.; Kaplan, D. L.; Omenetto, F. G.; Huang, Y.; Hwang, K.-C.; Zakin, M. R.; Litt, B.; Rogers, J. A. *Nat. Mater.* **2010**, *9*, 511–517.
- (38) Liu, Y.; Liu, J.; Chen, S.; Lei, T.; Kim, Y.; Niu, S.; Wang, H.; Wang, X.; Foudeh, A. M.; Tok, J. B. H.; Bao, Z. *Nat. Biomed. Eng.* **2019**, *3*, 58–68.
- (39) Sekitani, T.; Yokota, T.; Kuribara, K.; Kaltenbrunner, M.; Fukushima, T.; Inoue, Y.; Sekino, M.; Isoyama, T.; Abe, Y.; Onodera, H.; Someya, T. *Nat. Commun.* **2016**, *7*, 11425.
- (40) Khodagholy, D.; Doublet, T.; Quilichini, P.; Gurkinkel, M.; Leleux, P.; Ghestem, A.; Ismailova, E.; Hervé, T.; Sanaur, S.; Bernard, C.; Malliaras, G. G. *Nat. Commun.* **2013**, *4*, 1575.
- (41) Luan, L.; Wei, X.; Zhao, Z.; Siegel, J. J.; Potnis, O.; Tuppen, C. A.; Lin, S.; Kazmi, S.; Fowler, R. A.; Holloway, S.; Dunn, A. K.; Chitwood, R. A.; Xie, C. *Sci. Adv.* **2017**, *3*, No. e1601966.
- (42) Zhao, Z.; Li, X.; He, F.; Wei, X.; Lin, S.; Xie, C. *J. Neural Eng.* **2019**, *16*, 035001.
- (43) Schuhmann, T. G., Jr.; Yao, J.; Hong, G.; Fu, T.-M.; Lieber, C. M. *Nano Lett.* **2017**, *17*, 5836–5842.
- (44) Hong, G.; Fu, T.-M.; Zhou, T.; Schuhmann, T. G.; Huang, J.; Lieber, C. M. *Nano Lett.* **2015**, *15*, 6979–6984.
- (45) Wang, J.; Besnoin, E.; Duckham, A.; Spey, S.; Reiss, M.; Knio, O.; Powers, M.; Whitener, M.; Weihs, T. *Appl. Phys. Lett.* **2003**, *83*, 3987–3989.
- (46) Zhong, Z. *Microelectron. Reliab.* **2011**, *51*, 4–12.
- (47) Yim, M.-J.; Paik, K.-W. *IEEE Trans. Adv. Packag.* **1999**, *22*, 166–173.